Kinetic mass-transfer calculation of water isotope fractionation due to cloud microphysics in a regional meteorological model

I-Chun Tsai[1], Wan-Yu Chen[2,3], Jen-Ping Chen*[2,4], and Mao-Chang Liang[5]

1. Research Center for Environmental Changes, Academia Sinica, Taipei, Taiwan R. O. C.

2. Department of Atmospheric Sciences, National Taiwan University, Taipei, Taiwan, R.O.C.

3. Central Weather Bureau, Taipei, Taiwan, R.O.C.

4. International Degree Program on Climate Change and Sustainable Development, National Taiwan University, Taipei, Taiwan, R.O.C.

5. Institute of Earth Sciences, Academia Sinica, Taipei, Taiwan R. O. C.

* Corresponding Author:

Jen-Ping Chen, Professor

Department of Atmospheric Sciences

National Taiwan University

No. 1, Sect. 4, Roosevelt Road, Taipei, Taiwan 10673

Email: jpchen@ntu.edu.tw

Phone: +886-2-33663912Fax: +886-2-23633317

1   Abstract

2   In conventional atmospheric models, isotope exchange between liquid, gas and

3   solid phases is usually assumed to be in equilibrium, and the highly kinetic phase

4   transformation processes inferred in clouds are yet to be fully investigated. In this study,

5   a two-moment microphysical scheme in the NCAR Weather Research and Forecasting

6   (WRF) model was modified to allow kinetic calculation of isotope fractionation due to

7   various cloud microphysical phase-change processes. A case of moving cold front is

8   selected for quantifying the effect of different factors controlling isotopic composition,

9   including water vapor sources, atmospheric transport, phase transition pathways of

10   water in clouds, and kinetic versus equilibrium mass transfer. A base-run simulation

11   was able to reproduce the ~50‰ decrease in δD that observed during the frontal

12   passage. Sensitivity tests suggest that all the above factors contributed significantly to

13   the variations in isotope composition. The thermal equilibrium assumption commonly

14   used in earlier studies may cause an overestimate of mean vapor-phase δD by 11‰,

15   and the maximum difference can be more than 20‰. Using initial vertical distribution

16   and lower boundary conditions of water stable isotopes from satellite data are critical

17   to obtain successful isotope simulations, without which the δD in water vapor can be

18   off by about 34 and 28‰, respectively.   Without microphysical fractionation, the δD

19   in water vapor can be off by about 25‰.

20

1 Introduction

The water stable isotopes (^1H_2O, $^1H^2D^{16}O$ and $^1H_2^{18}O$) differ in molecular symmetry and weight. These differences in physical properties lead to a change in the stable isotope composition of water, due to fractionation during phase changes. When water vapor condenses and forms liquid or solid particles, it becomes depleted in ^2D and ^{18}O, because heavy isotopes condense preferentially to light ones. Information about the stable water stable isotopes is thus useful for understanding the water cycle (Dansgaard, 1964; Dawson and Ehleringer, 1998; Lorius et al., 1985; Risi et al., 2012; Sturm et al., 2010).

Isotope fractionation, as measured in precipitation, has been studied for decades. The observed isotope concentrations generally exhibit significant variations in either time or space. Factors such as surface type (e.g., land versus ocean), latitude, temperature, and precipitation amount effects are commonly considered to be key to the relationship between isotope fractionation and meteorological parameters (Dansgaard, 1964; Gonfiantini, 1985; Rozanski et al., 1993; Yurtsever and Gat, 1981; Kurita, 2013; Zwart et al., 2018). These factors are related to various physical processes, such as the surface water vapor source, atmospheric transport, phase changes in clouds and gravitational sorting of precipitation hydrometeors. For example, the water stable isotopic ratios decreased inland from the coast and the so-called continental effect (Clark and Fritz, 1997). The precipitation amount effect states that isotopic contents of tropical precipitation decrease as the amount of local precipitation increases (Dansgaard, 1964; Kurita, 2013), and the cause of which could be either the preferential removal during condensation (Cole et al., 1999; Yoshimura et al., 2003) or stronger downdraft in more intense convection (Risi et al., 2008). Untangling the intertwined effects of the various physical processes is essential to understanding isotope fractionation and the atmospheric water cycle.

47   The variations in isotope concentrations usually have multiple causes, and it is

48   difficult to understand the impacts of different factors by measurements alone.

49   Therefore, numerical models have been used to simulate isotope fractionation in the

50   atmosphere. The Rayleigh-type models, in which the air mass is continuously cooled

51   down and the condensation process is assumed to occur in isotopic equilibrium, are

52   widely used in discussing isotope measurements (Aldaz and Deutsch, 1967; Dansgaard,

53   1964). Such models can explain the linear relationship between the surface

54   temperature and isotopic composition of precipitation (Rozanski et al., 1993), and have

55   been expanded to incorporate more processes since the publication of Dansgaard

56   (1964). For example, Jouzel and Merlivat (1984) reported that the isotopic equilibrium

57   assumption led to an overestimation of the temperature-isotope gradients of polar

58   snow, so they included isotopic kinetic effects at snow formation in the models.

59   However, the Rayleigh-type models greatly simplify the complexity of the hydrological

60   cycle, and Joussaume et al. (1984) introduced the concept of building isotopes into an

61   atmospheric general circulation model (AGCM). AGCMs can calculate the transport

62   and mixing of air masses from different sources (which cannot be addressed by the

63   Rayleigh-type models), and have been used in studying the hydrological cycle in the

64   troposphere (Hoffmann et al., 1998; Lee et al., 2007; Sjolte and Hoffmann, 2014;

65   Yoshimura et al., 2008). In conventional AGCMs, isotope exchange between liquid or

66   ice and gas phases is usually assumed to be in a partial or full equilibrium state

67   (Hoffmann et al., 1998, Risi et al., 2010, Nusbaumer et al., 2017, Werner et al., 2011,

68   Yoshimura et al., 2010). In a synoptic weather system such as a front or typhoon,

69   thermal equilibrium fractionation may not be appropriate for describing fractionation

70   during phase change since the clouds are usually not in vapor equilibrium (Laskar et

71   al., 2014). Therefore, in recent years, several regional models start to consider the

72   kinetic fractionation during evaporation from open water, condensation from vapor

73 to ice, or isotope exchange from raindrops to unsaturated air (Hoffmann et al., 1998;

74 Yoshimura et al., 2010; Blossey et al. 2010; Pfahl et al., 2012; Dütsch et al., 2016).

75 However, the microphysics in these global or regional models are usually described

76 with single moment schemes. This study developed a kinetic fractionation scheme for

77 water stable isotopes using a two-moment microphysical scheme that coupled into the

78 National Center for Atmospheric Research (NCAR) Weather Research and Forecasting

79 (WRF) model (Skamarock, 2008) To understand the role of different factors in the

80 fractionation of the stable isotopes of water at the synoptic scale.

81 Because the α_{l-v} of ^{18}O (grey line in Fig. 2) does not deviate significantly from

82 unity, so the signal of ^{18}O fractionation is generally much less pronounced. Therefore,

83 we focus on deuterium for demonstrating the fractionation processes. The

84 microphysical processes of deuterium such as condensation and collision were

85 incorporated into WRF. A moving frontal system is selected to demonstrate the effect

86 of microphysical fractionation versus other controlling factors such as air mass origins

87 and surface sources. The effects of microphysical processes, including kinetic versus

88 equilibrium treatments, are discussed in more details; whereas the importance of

89 initial and boundary conditions of vapor-phase isotope is also investigated.

90
91 2   Methodology

92 In this study, the WRF model version 3.4.1 coupled with a two-moment bulkwater

93 microphysical scheme (cf. Cheng et al., 2010; Chen et al., 2015; Dearden et al., 2016)

94 that was developed at the National Taiwan University (hereafter, the NTU scheme) was

95 selected for simulations. The NTU scheme shown in Fig. 1 is modified to handle the

96 isotope fractionation due to various cloud microphysical phase-change processes.

97 The HDO cycle and their initial and boundary conditions were incorporated into the

98   model and more details were provided in section 2.1. The simulation setup and

99   observation data are given in section 2.2 and 2.3, respectively.

100

101   2.1   Description of the isotopic microphysical model

102   In modified NTU scheme, isotope mass transfer between vapor-, liquid-, and ice-

103   phase hydrometeors during microphysical processes such as deposition, sublimation,

104   evaporation, and condensation, were considered explicitly (cf. Fig. 1).   For processes

105   of collision-collection or melting/freezing, the masses of isotopes of the involving

106   particles are simply combined or conserved, respectively, without worrying about the

107   fractionation.

108   Thermal equilibrium fractionation has been widely used in conventional models.

109   In such schemes, the HDO concentration can be determined from the $H_2^{16}O$ (hereafter,

110   H_2O) concentration for both gas and liquid phases, because it is assumed that HDO is

111   always in equilibrium with H_2O, irrespective of their phase states. The equilibrium

112   between stable isotopes in liquid water and vapor phases is commonly expressed using

113   the isotopic fractionation factor α_{l-v}:

$$\alpha_{l-v} \equiv \frac{R_l}{R_v} \tag{1}$$

115   where R is the ratio of the heavy (HDO) to light (H_2O) isotopes. This ratio can be

116   explained with the Raoult's law, which states that the activity (saturation ratio) of each

117   species in the vapor phase equals its activity in the liquid phase. For the HDO–H_2O

118   system, this relationship can be expressed as:

$$\frac{n_{HDO}}{n_{HDO}+n_{H2O}+n_x} = \frac{P_{HDO}}{P_{s,HDO}} \tag{2a}$$

$$\frac{n_{H2O}}{n_{HDO}+n_{H2O}+n_x} = \frac{P_{H2O}}{P_{s,H2O}} \tag{2b}$$

121   where n is the number of moles in the liquid phase, P is vapor pressure, P_s is

122   saturation vapor pressure, whereas x represents all other chemical species.   By

123   dividing (2a) by (2b), one can derive the following:

124
$$\frac{\frac{n_{HDO}}{n_{H2O}}}{\frac{P_{HDO}}{P_{H2O}}} = \frac{P_{s,H2O}}{P_{s,HDO}}$$
(3)

125   One can see that the left-hand-side term is exactly α_{l-v}, while the right-hand-side

126   term tells us that this factor is actually the ratio between the saturation vapor pressure

127   of H_2O and HDO.   Thus the isotopic fractionation factor α_{l-v} is a function of

128   temperature only, and can be determined experimentally.   In this study, we adopted

129   the temperature dependence of α_{l-v} from Horita and Wesolowski (1994):

130
$$10^3 \cdot ln\alpha_{l-v} = 1158\left(\frac{T^3}{10^9}\right) - 1620.1\left(\frac{T^2}{10^6}\right) + 794.84\left(\frac{T}{10^3}\right) - 161.04 + 2.9992(\frac{10^9}{T^3})$$ (4a)

131

132   whereas that between ice and water vapor was adapted from Ellehoj et al. (2013).

133
$$ln\alpha_{s-v} = ln\frac{R_s}{R_v} = 0.2133 - \frac{203.10}{T} + \frac{48888}{T^2}$$
(4b)

134   where the subscript "s" means solid phase.

135   When kinetic process is considered, isotopic fractionation is not only related to

136   temperature but also factors such as the diffusion coefficient and water vapor

137   concentration.   The   calculation   of   kinetic   fractionation   during

138   condensation/evaporation is based on the two-stream Maxwellian kinetic equation:

139
$$\frac{dm_{HDO}}{dt} = 4\pi r D_{HDO}\left(\rho_{env,HDO} - \rho_{p,HDO}\right)$$
(5)

140   where m is HDO mass in the particle, t is time, r is hydrometeor particle size, D

141   is the mass diffusivity in air, ρ_{env} is vapor density in the air, and ρ_p is vapor density

142   at the particle surface. The latter two terms can be rewritten as:

143
$$\rho_{env,HDO} = \frac{P_{HDO}}{R_{HDO}T_{air}} \text{ and } \rho_{p,HDO} = a_{HDO}\frac{P_{s,HDO}}{R_{HDO}T_p}$$
(6)

144   where R_{HDO} is the gas constant of HDO; a_{HDO} and $P_{s,HDO}$ are the activity and

145   saturation vapor pressure of HDO, respectively; and T_{air} and T_p are temperatures

146   of air and particle surface, respectively.   Equation (5) is for single particle, but the

147   bulkwater microphysical schemes commonly used in regional weather models deal

148   with a population of hydrometeor particles (thus called bulkwater). Conventional

149   bulkwater schemes apply a mathematical function to represent the size distribution of

150   any hydrometeor category, and the matnematical function is solve by knowing several

151   bulk properties (moments) of the size distribution. The NTU scheme is a two-moment

152   scheme that predicts both the number and mass concentrations of each bulkwater

153   category, which allows better presentation of microphysical processes than the

154   commonly used one-moment schemes (Taufour et al., 2018). In contrast to the

155   conventional bulkwater schemes that must assume a certain size distribution function,

156   the NTU scheme derived the warm-cloud parameterization by analyzing results from

157   bin model simulations and thus is rather accurate and comprehensive in microphysical

158   processes; while the cold-cloud parameterization still follows the conventional

159   approach. Another advantages of the NTU scheme is that it does not apply the

160   "saturation adjustment" strategy, as done in most global and regional models. This

161   saturation adjustment treatment assumes that water vapor and liquid (or ice) water

162   are in thermodynamic equilibrium once water (or ice) saturation is reached in non-

163   mixed-phase clouds (i.e., all hydrometeors are either liquid or ice). Therefore, for

164   models applying the saturation adjustment strategy, condensation is not calculated

165   explicitly but rather by converting all excess water vapor into condensate regardless of

166   the cloud drop size and number concentration or the time needed for condensing out

167   all supersaturated water. So, under the saturation adjustment assumption, kinetic

168   effect as described in Eq. (5) cannot be solved fully and explicitly. In mixed-phase

169   clouds (i.e., water and ice coexist), the equilibrium is maintained by assuming either

170   water saturation or ice saturation (e.g., Sundqvist, 1978), or by varying linearly from

171   water saturation to ice saturation between two specified temperature thresholds (e.g.,

172   Tiedtke, 1993).   Then, condensation on ice can be calculated following the kinetic

173   approach, but the condensation on cloud drops still follows the saturation adjustment

174   in most models.   If the air is subsaturated but with the presence of cloud drops (or

175   cloud ice), the cloud drops (or cloud ice) are forced to evaporate to maintain the

176   equilibrium until they are all evaporated. As the saturation adjustment strategy

177   conventionally is not applied in subsaturated conditions for precipitation particles (e.g.,

178   raindrops, snow, etc.), it should be denoted as a partial equilibrium assumption.

179   The kinetic effect might have significant impacts on isotope fractionation and thus

180   there is a need to be considered in models.   For example, Hoffmann et al. (1998) tried

181   to consider the kinetic effect during deposition growth in the ECHAM AGCM model.

182   Due to the saturation adjustment assumption in ECHAM model, an effective factor,

183   which is function of temperature only, is used to express the kinetic effect (Jouzel and

184   Merlivat, 1984). In Wernet et al. (2011), the condensation on ice is also calculated with

185   an effective factor, but the condensation on cloud drops is in equilibrium fractionation.

186   In reality, deviation from equilibrium is rather common in cloud, and its magnitude

187   depends on factors such as updraft speed and hydrometeors' size spectra. These

188   factors usually are not considered in existing models but are included in the NTU

189   scheme.

190   Key parameters such as the HDO saturation vapor pressure, $P_{s,HDO}$, and diffusion

191   coefficient, D_{HDO} are modified to handle HDO in the NTU scheme.   The HDO

192   saturation pressure, which is needed for the kinetic mass transfer calculation in Eq. (5),

193   can be obtained by equating Eq. (3) to Eq. (4). The derived HDO saturation vapor

194   pressure is generally lower than that of H_2O, and the differences increase as

195 temperature gets lower (Fig. 2). The mass diffusivity of HDO in air, D_{HDO}, in Eq. (5)

196 was obtained based on the relationship proposed by Hirschfelder et al. (1954):

$$D_x \propto \frac{m_{Air}+m_x}{m_{Air}m_x} \qquad (7)$$

198 where x represents any gas molecule.   Assuming that the proportionality

199 constants are the same for D_{HDO} and D_{H_2O}, one can obtained the following:

$$\frac{D_{HDO}}{D_{H_2O}} = \frac{\frac{m_{Air}+m_{HDO}}{m_{Air}m_{HDO}}}{\frac{m_{Air}+m_{H_2O}}{m_{Air}m_{H_2O}}} \cong 0.9676 \qquad (8)$$

201 with which we can relate D_{HDO} to D_{H_2O}.

202   In Eq. (6), the activity of water stable isotope depends on the composition of the

203 particle.   For ice particles, the model cannot trace the history of water stable isotope

204 deposition and thus cannot distinguish between the surface layer from the inner core

205 of the ice particles.   Therefore, the water stable isotope activity of ice-phase

206 hydrometeor is assumed to depend on its bulk composition (i.e., assuming well-mixed).

207 In reality, however, there is no homogenization of isotopes in ice particles due to the

208 low diffusivities of molecules in ice.   Blossey et al. (2010), Pfahl et al. (2012) and

209 Dütsch et al. (2016) dealt with this problem by setting the ice particle's isotope ratio

210 equal to that produced by vapor deposition. This is an effective approach as only the

211 most recently deposited ice is exposed to the vapor. However, during evaporation the

212 mass exchange depends heavily on the residual composition, making the treatment

213 rather tricky. Before a better solution is devised, this study adopted the bulk

214 composition approach for both condensation and evaporation processes.

215 2.2   Simulation Setup

216   Frontal systems are not only rich in cloud microphysical processes but also involve

217 air-mass transitions and atmospheric circulation. As a result, they are ideal for

218 evaluating the relative contribution of various physical processes to isotopic

219 fractionation. The case selected for this study is a frontal system that passed through

220 northern Taiwan on 11 June 2012, with moderate to heavy rainfall from the night of

221 11 June until noon on 12 June. Special focus will be placed on northern Taiwan because

222 of the availability of isotope measurements for verification.

223 The simulation domain is shown in Fig. 3. The resolution of the coarse domain

224 was set at 81 km, covering the region from 90° to 150°E and 0° to 50°N. The resolutions

225 of the nested domains were set at 27 km, 9 km, and 3 km. The innermost domain

226 covers Taiwan and the surrounding ocean. Twenty-eight vertical layers were used,

227 eight of which were below 1.5 km (roughly the height of the planetary boundary layer),

228 with a maximum model height at 50 hPa. For the initial and boundary conditions, we

229 applied the National Centers for Environmental Prediction (NCEP) Final Global analysis

230 (FNL) data with a 1° by 1° resolution. FNL data for wind properties and temperatures

231 were nudged into domains 1 and 2 only every 6 h for better simulation of the

232 meteorology.   The physical options used in the WRF model included the NTU

233 microphysical scheme, the rapid radiative transfer model (RRTM) longwave and

234 shortwave radiation scheme (Mlawer et al., 1997), and the Yonsei University (YSU)

235 planetary boundary layer scheme (Hong et al., 2006). Cumulus parameterization was

236 turned off in the simulations.

237 To examine different factors that control the water stable isotopes concentration,

238 six simulations were conducted: the control run (CTRL) used the kinetic approach for

239 cloud microphysical processes; the EQ run used the thermal equilibrium approach;

240 NoIce was conducted to examine the differences between liquid- and ice-phase

241 fractionations; NoLnd inspects land-sea contrast of water vapor sources; and NoVh is

242 for investigating the vertical exchange of isotope composition between lower and

243   upper troposphere. We also conducted a blank test (NoFrac) in which isotopic

244   microphysical fractionation was turned off. Descriptions of these numerical

245   experiments is listed in Table 1.

246   The isotopic value for water vapor or condensates is conventionally expressed as

247   δD (conventionally expressed in ‰):

248    $$\delta D = \left(\frac{R}{R_{SMOW}} - 1 \right) \tag{9}$$

249   where R is the $\frac{HDO}{H_2O}$ ratio in the sample, and R_{SMOW} is the Vienna Standard Mean Ocean

250   Water isotopic ratio (Craig, 1961).   The lower boundary condition of δD over land

251   and ocean are calculated by relating HDO flux to H_2O flux according to Eqs. (3) and (4).

252   In such a conversion, the ratio R_l over land is set to be that in surface precipitation

253   according to observed mean climatology in June from the Global Network of Isotopes

254   in Precipitation (GNIP) (Johnson and Ingram, 2004; Rozanski et al., 1993). The obtained

255   initial near-surface distribution of water vapor δD (δD_V) is shown in Fig. 4a.

256   The vertical distribution of initial atmospheric water stable isotope

257   concentrations (Fig. 4b) was obtained from the NASA TES-Aura level-3 data

258   (http://tes.jpl.nasa.gov/data/products/).   We took the data for the month of June

259   and averaged over years 2006-2012.   Although the concentrations of water vapor (QV)

260   and HDO (QIV) usually decrease exponentially with height, their ratios (i.e., QV:QIV)

261   vary rather linearly with height.   So, for areas over land, the vertical profile is fitted

262   as the following:

263    $$QIV(z) = \left(\frac{QIV_{srf}}{QV_{srf}} \right) \cdot (-4.940699 \cdot 10^{-5} \cdot z + 1.128299) \cdot QV(z) \tag{10a}$$

264   where QIV_{srf} and QV_{srf} are near surface value of QIV and QV, respectively.   For

265   marine environments, the profile is fitted as:

12

266
$$QIV(z) = (\frac{QIV_{srf}}{QV_{srf}}) \cdot (-5.005261 \cdot 10^{-5} \cdot z + 1.134024) \cdot QV(z) \qquad (10b)$$

267 Note that these formulas apply only to the free troposphere; within the planetary

268 boundary layers, QIV is assumed to be well mixed (see Fig. 4b for the full profiles).

269

270 2.3 Observations

271   The isotopic water vapor and rainwater δD data from 11–12 June, 2012, were

272 recorded using a cavity ring-down spectroscopy analyzer (CARDS, Picarro L2120-i),

273 following Gupta et al. (2009). The measurement of rainwater was conducted on the

274 fourth floor of the building of the Department of Geography, National Taiwan

275 University (NTU, 25.02°N, 121.53°E). The isotopic water vapor measurements were

276 conducted at Academia Sinica (AS), which is about 10 km east of the rainwater

277 collection site. The two sites are marked as N and A, respectively, in Fig. 5a. The

278 uncertainties in δD for liquid and vapor samples were found to be less than 0.3‰ and

279 1.0‰, respectively (Laskar et al., 2014). The precision of water vapor concentration

280 measurements made using a Picarro CRDS is less than 100 ppmv (Crosson, 2008); this

281 is applicable to all of the data presented here. In addition to these experimental data,

282 the NCEP Reanalysis II (R2) data and precipitation data from the Central Weather

283 Bureau of Taiwan (https://www.cwb.gov.tw/eng/index.htm) were used to verify the

284 simulations. Unfortunately, the NASA TES-Aura satellite daily data during this case not

285 available for verification over the studied region.

286

287 3 Results

288 3.1 Model verification

289   Comparison of the model results with the NCEP R2 data shows that the model

290 captured the locations of the cold front and associated low-pressure system

291   reasonably well; the front was over the East China Sea on 11 June and moved to Taiwan

292   on 12 June (Fig. 6). However, the simulated precipitation was generally lower than

293   observed, especially over northwestern Taiwan (Fig. 5a). Additionally, the first peak in

294   rainfall during the early morning of 11 June (Fig. 5b), was not obvious in the simulated

295   results. The impact of these discrepancies will be discussed in section 4.

296   The observed δD_V was about −90~−120‰ during the pre- and post-frontal

297   periods, and decreased to a minimum of −160‰ on 12 June. The simulated δD_V

298   (−70~−100‰) were about 20‰ higher than observed during the pre- and post-frontal

299   periods (Fig. 7), whereas the minimum δD_V of −150‰ was slightly higher than the

300   observed during the rainy period. Observation of δD in precipitation (δD_L) was

301   available only after 09:00 (local time) on 12 June (Fig. 7b). It decreased slightly from -

302   70 to −90‰ before 16:00 and then recovered to around −30‰ by the evening of 12

303   June. The simulated minimum is also around −90‰, but occurred a few hours earlier

304   than observed. The classic amount effect cannot be assessed from

305   observations. For model simulations, the simulated δD in precipitation (Fig. 7b)

306   decreased with precipitation occurred (Fig. 5b).   The negative correlation is similar to

307   the amount effect in other studies. Overall, the model captured reasonably well the

308   pattern and magnitude of changes in δD during the frontal passage, except that the

309   timing is off by a few hours.

310

311   3.2   Factors affecting isotopic fractionation

312   The simulated spatial distribution of δD_V in Fig. 8a and 8d show two main zones

313   of minimum δD_V, one over mid-latitudes and the other over the latitudes of Taiwan.

314   The former is mainly due to low δD of surface vapor source (cf. Fig. 4a); whereas the

315   latter is associated with the frontal rainband, and corresponds to the observed minima

316   shown in Fig. 7a.   At a first glance, one may deduce two main causes for the minima.

14

317   Firstly, the near-surface air in the frontal zone is basically of continental origin, where

318   the δD_V is lower than over the oceans (cf. Fig. 4a). Secondly, precipitation microphysics

319   inside the frontal system caused a strong reduction (fractionation) in δD of

320   hydrometeors as can be seen in Figs. 8e and 8f; therefore, the evaporation of

321   hydrometeors would produce low δD_V in the lower troposphere.   The above results

322   are in agreement with the finding of Dütsch et al. (2016), who pointed out that

323   horizontal transport determines the large-scale pattern of water stable isotope in both

324   vapor and precipitation, while fractionation and vertical transport are more important

325   on a smaller scale, near the fronts. Note that the location of the hydrometeor's δD

326   minima at 500hPa and 850hPa is shifted due to the structure of the frontal system.

327   However, the relatively high δD_V behind (to the north of) the frontal system may seem

328   a bit strange, as the air mass there should be of continental origin.   This suggests

329   more complicated mechanisms.   Besides the water vapor source and microphysical

330   fractionation, other factors such as the initial vertical distribution may also contribute

331   to the variation in δD values. So, in order to decipher all possible controlling factors

332   and to evaluate their relative contributions, we need to examine results from the 5

333   sensitivity experiments that listed in Table 1.

334   The most obvious differences between the CTRL and other simulations in terms

335   of δD in the vapor (δD_V) and liquid (δD_L) phases at 850 hPa occurred near the front

336   because that is the location of the richest microphysical fractionation and largest

337   contrast in air mass properties (Fig. 9). Isotopic fractionation due to phase change in

338   the CTRL run was weaker than that calculated in the EQ run (Fig. 9a), because the

339   isotopic compositions were not always in equilibrium between the different phases in

340   the CTRL run. That led to slower isotopic fractionation under severe phase changes.

341   The vertical distribution of δD_V between the CTRL and EQ runs over northern

342 Taiwan (121-123°E, 25-27°N) is shown in Fig. 10a. The differences in water vapor δD at

343 around 850 hPa or higher prior to the passing of the front (point A, Fig. 10a) are

344 associated with cloud formation due to mesoscale lifting in the warm air sector. When

345 the frontal system passed through northern Taiwan in the early morning of 12 June,

346 low δD_L extended almost down to the surface. The δD_L in the EQ run was about 30‰

347 lower than that in the CTRL run during this period. These results suggest that the

348 equilibrium assumption may lead to large biases in δD for a synoptic-scale weather

349 system as mentioned in other studies (e.g., Risi et al., 2010), and kinetic calculation is

350 crucial to isotope modeling.

351 The degree of isotopic fractionation is related to temperature. As the ratio

352 between the saturation pressure of H_2O and HDO in different phases deviate more

353 from unity at lower temperatures (cf. Fig. 2), higher degree of fractionation will occur

354 at lower temperatures. The significance of ice-phase fractionation is tested with the

355 NoIce run, for which the saturation vapor pressure of ice-phase HDO was assumed to

356 be the same as that of the liquid phase, which leads to weaker HDO vapor deposition

357 on ice. The resulting differences in δD_V are small near the surface (Figs 9b and 10b) but

358 become significant at higher altitudes where the ice fractionation deviate more from

359 that of liquid. Reduced δD in the ice phase (δD_I) can be seen immediately above the

360 0°C level (Fig. 10b), causing more heavy water isotopes to remain in the gas phase and

361 then transport to higher altitudes. This results in an elevated δD in both the vapor and

362 the ice phase. The increase in δD_V and δD_I can reach over 50‰ and 30‰, respectively,

363 near the tropopause. Such changes may also affect the lower troposphere, because

364 snow and graupel particles may fall to lower levels and bring down high δD_I water.

365 The amount of changes due to such gravitational sorting depends on whether

366 snow/graupel were formed in the lower or higher mixed-phase zone; the former leads

367 to lower δD_I, while the latter increases it. However, the changes were generally within

368   10‰. Due to the temperature dependence of the isotopic value and the structure of

369   the atmosphere, ignoring the difference between liquid and ice-phase fractionations

370   will lead a vertical redistribution of the isotopes.

371   The initial and boundary conditions are also important in determining the isotope

372   levels. Based on the IAEA data, precipitation δD decreases from marine to inland areas,

373   indicating that the water source is important in determining the initial water stable

374   isotope content. In the NoLnd run, the initial δD over land was set to be the same as

375   that over the ocean, and this resulted in a higher δD not only over land but also in the

376   frontal system (Fig. 9c). Ahead of the front, the vapor-phase δD in the NoLnd run

377   increased by about 40‰ relative to the CTRL run. The initial vertical distribution of δD_V,

378   which was based on satellite data, showed large vertical decay into the free

379   troposphere. In the NoVh run, the initial δD in the free troposphere is assumed to be

380   the same as that in the planetary boundary layer. This caused 20-50‰ overestimation

381   of δD_V at near surface (Fig. 9d).

382   When the observed and simulated δD_V at AS and precipitation δD_L at NTU are

383   compared (Fig. 11), one can see that the full simulation (i.e., the CTRL run, red line) is

384   rather close to the observation in terms of the peak values during the time of frontal

385   passage (06:00-12:00 LST on June 12). In contrast, the decrease in δDV was

386   overestimated by 11‰ in the equilibrium run and underestimated by 28 and 34‰ in

387   the NoLnd, and NoVh runs, respectively. The simulated δD_V in the NoIce run is rather

388   close to that in the CTRL run, which is consistent with the vertical profile shown in Fig.

389   10b, suggesting that the ice-phase process does not have a significant effect on δD at

390   lower altitudes; however, the changes in the upper troposphere are significant. The

391   importance of microphysical fractionation is elucidated with the NoFrac run (grey line

392   in Fig.11), which yields 25‰ and more than 50‰ differences in the minimum δD_V; and

393   δD_I, respectively.

394

395 4   Discussion

396   Combining the observations and simulations results   of the water stable

397 isotopes can be used to understand the water cycle. From the observed δD_V decreased

398 after 06:00 on 12 June (black line in Fig. 11), much later than the onset of the

399 precipitation. The observations suggested that the source of water vapor before this

400 time is the ocean (Wang et al., 2016) and that the microphysical processes related to

401 the precipitation did not substantially affect δD_V during this period.   Model

402 simulations can help with further understanding of such isotopic fractionation. The

403 δD_V on 11 June varied little among different tests (Fig, 11) because the airmass was

404 from nearby areas (i.e., no significant advection effect) and no cloud microphysical

405 processes occurred during this period.   However, water vapor δD_V decreased from -

406 80 to -100‰ at midnight of 11-12 June in the control run, but not in the NoLnd run,

407 indicating that the decreases in δD_V was due to advection of the continental airmass.

408 When the front passed through during the early morning of 12 June, δD_V decreased

409 from −100 to −170‰ in the control run but not in the NoFrac run (grey line in Fig.10),

410 indicating that the additional differences was caused by cloud microphysical processes.

411 After the passage of frontal system, δD_V returned to its background level, around

412 −80‰. The results of these sensitivity tests suggest that the changes in δD_V due to

413 cloud microphysical processes, initial vertical distribution, and lower boundary

414 conditions are of a similar order, and are all important to isotopic fractionation.

415   Although the model seems to adequately reproduced changes in δD in this frontal

416 case, there are some minor inconsistencies between the simulation results and

417 observations. Some discrepancies originated from the meteorological model itself and

418 the initial meteorological conditions, which caused inaccuracies in the intensity or

419 timing of surface precipitation. In fact, most models including ours failed to simulate

18

420　the strong precipitation over land for this system (Wang et al. 2016). The observed

421　water vapor and precipitation δD values were not in phase, and the water vapor δD

422　decreased prior to precipitation (black line in Fig. 11). In contrast, the decreases in the

423　simulated precipitation and water vapor δD were almost simultaneous, starting

424　around 03:00 on 12 June (red line in Fig. 11). This again suggests that the model missed

425　an earlier local convection system occurred during the early morning, such that the

426　simulation can reflect only the δD variation due to the frontal system. The simulated

427　δD_V decreased and returned to its previous level earlier than the observed δD_V

428　(~03:00-10:00 compared to ~07:00 -13:00). This also suggests that the arrival time of

429　the frontal system to Taipei was earlier than observed, although the speed of the

430　simulated system was close to that of the observed one, taking about seven hours to

431　pass through Taipei.

432　　Uncertainties may also exist in the observation data, as the vapor and

433　precipitation measurements were taken at different locations, separated by about 10

434　km.　A comparison of precipitation at different sites (Fig. 12; NanGang station is close

435　to AS, and GongGuan station is close to NTU) suggests that the difference in sampling

436　locations would not significantly affect the results in this study. Another uncertainty is

437　the parameterization of isotopic fractionation factor α. In this study, the temperature

438　dependence of α_{l-v} and α_{s-v} were adopted from Horita and Wesolowski (1994)

439　and Ellehoj et al. (2013) , respectively.　In most models, the formulation for ice/vapor

440　by Merlivat and Nief (1967) is still used. From Fig. 2 one can estimated that the

441　differences in α_{s-v} between Ellehoj et al. (2013) and Merlivat and Nief (1967) are

442　around 1% between -10~-20°C and 4% at -40°C; whereas the differences of

443　α_{l-v} between Horita and Wesolowski (1994) and Merlivat and Nief (1967) are less

444　than 1%.

445　　There are also uncertainties in the treatment of microphysical processes. The

446   isotopic value for water vapor at the lower boundary condition was assumed to be in

447   equilibrium with surface precipitation in this study. Rangarajan et al. (2017) analyzed

448   the isotopic ratios in water vapor from measurements over Taipei, and they found that

449   isotopic values were not always in equilibrium. This suggests that the assumed lower

450   boundary condition might not always be applicable for Taipei. Moreover, since the

451   lower boundary condition can be affected by fresh precipitation, δD_V might decrease

452   after the precipitation event which brings in low δD_L to the soil; yet, our model does

453   not update the surface δD_V flux accordingly.   This might partially explain the

454   discrepancy in δD_V after the frontal passage that shown in Fig. 7a. In addition, the

455   evaporation from the ocean is assumed as in equilibrium between liquid and vapor

456   phases. This assumption may also affect the simulation of δD in the model, and the

457   process needs to be explicitly considered in the future study. Finally, whether the

458   nonequilibrium effects are important for the second-order isotope parameter,

459   deuterium excess, is an interesting subject worthy of further investigation by including

460   the description of $\delta^{18}O$ isotope in the model.

461

462   5   Conclusion

463   Exploring physical processes controlling the stable isotopic composition of water,

464   including details such as water vapor source, atmospheric circulation, and cloud

465   microphysical processes, is useful for understanding the water cycle. In this study, we

466   modified the NCAR WRF model to understand the role of different factors in the

467   fractionation of the stable isotopes of water. The experimental stable isotope thermal

468   equilibrium data were converted into isotope saturation vapor pressure, which was

469   then used in the two-stream Maxwellian kinetic equation for calculating the

470   condensation/evaporation or deposition/sublimation of HDO, in parallel with that for

471   H_2O. Mass conservation was also considered explicitly for the collection processes as

472   well as during freezing/melting.

473   A frontal system event was selected to reveal the complexity of isotope

474   fractionation. The model captured the location of the front adequately, although the

475   estimated precipitation was less than observed. The simulated results showed fairly

476   good agreement with water vapor and rainwater stable isotope measurements, and

477   suggested that the decreases in water vapor δD before the front arrived in Taiwan was

478   due to an airmass of continental origin. When the front passed during the early

479   morning of 12 June, both the water vapor sources and the cloud microphysical

480   processes contributed to a decrease in water vapor δD, which returned to a

481   background levels after the front had passed.

482   Additional sensitivity experiments showed that the thermal equilibrium

483   assumption commonly used in earlier studies might significantly overestimate the

484   decrease of mean δD by about 11‰, while the maximum difference can be more than

485   20‰, during the precipitation event. Cloud microphysical processes, including ice-

486   phase processes, have substantial effects on isotopic fractionation, especially on the

487   vertical redistribution of isotopes.   Furthermore, the sensitivity tests suggest that the

488   initial vertical profile and the land–sea contrast in surface sources are quite important

489   in simulating atmospheric stable isotopic composition, and should be estimated from

490   observations such as satellite data, without which the underestimation in the decrease

491   of water vapor δD could reach about 34 and 28‰, respectively. The problem in

492   determining the activity of water stable isotope in ice particles without knowing the

493   inhomogeneity of chemical composition in the bulk ice, as mentioned at the end of

494   section 2.1 is another issue worthy of further study. To accommodate the different

495   conditions between condensation and evaporation, it might be feasible to assume that

496   the water stable isotope activity is determined by the vapor phase during

497   condensation following the approach of Blossey et al. (2010), Pfahl et al. (2012) and

498   Dütsch et al. (2016); whereas for the evaporation process, one may assume a well-

499   mixed bulk composition for determining the isotope activity as done in this study. In

500   summary, this study suggests that a better understanding in the relationship between

501   water stable isotope variation and hydrological cycle can be achieved with a

502   combination of multi-platform observations and detailed cloud model simulations.

503

507

References

Aldaz, L., and Deutsch, S.: On a relationship between air temperature and oxygen isotope ratio of snow and firn in the south pole region, Earth and Planetary Science Letters, *3*(Supplement C), 267-274, 1967.

Blossey, N. P., Kuang, Z. and Romps, D. M.: Isotopic composition of water in the tropical tropopause layer in cloud-resolving simulations of an idealized tropical circulation. J. Geophys. Res., 115. https://doi.org/10.1029/2010JD014554, 2010.

Chen, J. P., and Liu, S. T.: Physically based two-moment bulkwater parametrization for warm-cloud microphysics, Quarterly Journal of the Royal Meteorological Society, *130*(596), 51-78, 2004.

Chen, S. H., Liu, Y. C., Nathan, T. R., Davis, C., Torn, R., Sowa, N., Cheng, C. T., and Chen, J. P.: Modeling the effects of dust-radiative forcing on the movement of Hurricane Helene (2006), Q.J.R. Meteorol. Soc., 141: 2563-2570, 2015.

Cheng, C.-T., Wang, W.-C., and Chen, J.-P.: A modeling study of aerosol impacts on cloud microphysics and radiative properties, Q.J.R. Meteorol. Soc., 133(623B), 15, 2007.

Cheng, C.-T., Wang, W.-C., and Chen, J.-P.: Simulation of the effects of increasing cloud condensation nuclei on mixed-phase clouds and precipitation of a front system, Atmospheric Research, 96(2–3), 461-476, 2010.

Clark, I., and Fritz, P.: Environmental Isotopes in Hydrogeology. Boca Raton: CRC Press, 1997.

Cole, J. E., Rind, D., Webb, R. S., Jouzel, J., and Healy, R.: Climatic controls on interannual variability of precipitation δ18O: Simulated influence of temperature, precipitation amount, and vapor source region, J. Geophys. Res., 104, 14,223–14,236, 1999.

Craig, H.: Isotopic Variations in Meteoric Waters, Science, *133*(3465), 1702-1703, 1961.

Crosson, E. R.: A cavity ring-down analyzer for measuring atmospheric levels of methane, carbon dioxide, and water vapor, Applied Physics B, 92(3), 403-408, 2008.

Dansgaard, W.: Stable isotopes in precipitation, Tellus, *16*(4), 436-468, 1964.

Dawson, T. E., and Ehleringer, J. R.: Plants, isotopes and water use: a catchment-scale perspective, Isotope tracers in catchment hydrology, 165-202, 1998.

Dearden, C, Vaughan, G., Tsai, T.-C., and Chen, J.-P.: Exploring the diabatic role of ice microphysical processes in UK summer cyclones. Mon. Wea. Rev., 144, 1249-1272, 2016.

Dütsch, M., Pfahl, S., and Wernli, H.: Drivers of δ^2H variations in an idealized extratropical cyclone, Geophys. Res. Lett., 43, 5401–5408, 2016.

Ellehoj, M., Steen-Larsen, H. C., Johnsen, S. J., and Madsen, M. B.: Ice-vapor equilibrium fractionation factor of hydrogen and oxygen isotopes: Experimental investigations and implications for stable water isotope studies, Rapid

546   Communications in Mass Spectrometry, 27(19), 2149-2158, 2013.

547   Gonfiantini, R. : On the isotopic composition of precipitation in tropical stations (*),
548   Acta Amazonica, 15(1-2), 121-140, 1985.

549   Gupta, P., Noone, D., Galewsky, J., Sweeney, C., and Vaughn, B. H.: Demonstration of
550   high-precision continuous measurements of water vapor isotopologues in
551   laboratory and remote field deployments using wavelength-scanned cavity ring-
552   down spectroscopy (WS-CRDS) technology, Rapid communications in mass
553   spectrometry, 23(16), 2534-2542, 2009.

554   Hirschfelder, J. O., Curtiss, C. F., Bird, R. B., and Mayer, M. G.: Molecular theory of gases
555   and liquids, Wiley New York, 1954.

556   Hoffmann, G., Werner, M., and Heimann, M.: Water isotope module of the ECHAM
557   atmospheric general circulation model: A study on timescales from days to
558   several years, J. Geophys. Res., 103(D14), 16871-16896, 1998.

559   Hong, S.-Y., Noh, Y., and Dudhia, J. : A New Vertical Diffusion Package with an Explicit
560   Treatment of Entrainment Processes, Monthly Weather Review, 134(9), 2318-
561   2341, 2006.

562   Horita, J., and Wesolowski, D. J.: Liquid-vapor fractionation of oxygen and hydrogen
563   isotopes of water from the freezing to the critical temperature, Geochimica et
564   Cosmochimica Acta, 58(16), 3425-3437, 1994.

565   Johnson, K. R., and Ingram, B. L.: Spatial and temporal variability in the stable isotope
566   systematics of modern precipitation in China: implications for paleoclimate
567   reconstructions, Earth and Planetary Science Letters, 220(3), 365-377, 2004.

568   Joussaume, S., Sadourny, R., and Jouzel, J.: A general circulation model of water isotope
569   cycles in the atmosphere, Nature, 311, 24, 1984.

570   Jouzel, J., and Merlivat, L.: Deuterium and oxygen 18 in precipitation: Modeling of the
571   isotopic effects during snow formation, J. Geophys. Res., 89(D7), 11749-11757,
572   1984.

573   Kurita, N.: Water isotopic variability in response to mesoscale convective system over
574   the tropical ocean, J. Geophys. Res., 118, https://doi.org/10.1002/jgrd.50754,
575   2013.

576   Laskar, A. H., Huang, J.-C., Hsu, S.-C., Bhattacharya, S. K., Wang, C.-H., and Liang, M.-C.:
577   Stable isotopic composition of near surface atmospheric water vapor and rain–
578   vapor interaction in Taipei, Taiwan, Journal of Hydrology, 519, 2091-2100, 2014.

579   Lee, J.-E., Fung, I., DePaolo, D. J., and Henning, C. C.: Analysis of the global distribution
580   of water isotopes using the NCAR atmospheric general circulation model, J.
581   Geophys. Res., 112(D16) , https://doi.org/10.1029/2006JD007657, 2007.

582   Lorius, C., Ritz, C., Jouzel, J., Merlivat, L., and Barkov, N.: A 150,000-year climatic record
583   from Antarctic ice, Nature, 316, 591-596, 1985.

584 Merlivat L, and Nief, G.: Fractionnement isotopique lors des changements d'etat ´
585   solide-vapeur et liquide-vapeur de l'eau a des temp `eratures inf´erieures ´a 0 `
586   ◦C. Tellus 19:122–127, 1967.

587 Mlawer, E. J., Taubman, S. J., Brown, P. D., Iacono, M. J., and Clough, S. A.: Radiative
588   transfer for inhomogeneous atmospheres: RRTM, a validated correlated-k model
589   for the longwave, J. Geophys. Res., 102(D14), 16663-16682, 1997.

590 Pfahl, S., Wernli, H., and Yoshimura, K.: The isotopic composition of precipitation from
591   a winter storm – a case study with the limited-area model COSMOiso. Atmos.
592   Chem. Phys., 12, 1629–1648, 2012.

593 Rangarajan, R., Laskar, A. H., Bhattacharya, S. K., Shen, C.-C., and Liang, M.-C.: An
594   insight into the western Pacific wintertime moisture sources using dual water
595   vapor isotopes, Journal of Hydrology, 547, 111-123, 2017.

596 Risi, C., et al.: Process-evaluation of tropospheric humidity simulated by general
597   circulation models using water vapor isotopologues: 1. Comparison between
598   models and observations, J. Geophys. Res., 117(D5), D05303, 2012.

599 Rozanski, K., Araguás-Araguás, L., and Gonfiantini, R.: Isotopic Patterns in Modern
600   Global Precipitation, in Climate Change in Continental Isotopic Records, edited,
601   pp. 1-36, American Geophysical Union, https://doi.org/10.1029/GM078p0001,
602   1993.

603 Sjolte, J., and Hoffmann, G.: Modelling stable water isotopes in monsoon precipitation
604   during the previous interglacial, Quaternary Science Reviews, 85, 119-135, 2014.

605 Skamarock, W. C., Klemp, J. B., Dudhia, J., Gill, D. O., Barker, D. M., Duda, M., Huang,
606   X.-Y., Wang, W. and Powers, J. G. : A Description of the Advanced Research WRF
607   Version 3, NCAR Technical Note, 2008.

608 Sturm, C., Zhang, Q., and Noone, D. : An introduction to stable water isotopes in
609   climate models: benefits of forward proxy modelling for paleoclimatology,
610   Climate of the Past, 6(1), 115-129.

611 Taufour, M., Vié, B., Augros, C., Boudevillain, B., Delanoë, J., Delautier, G., Ducrocq, V.,
612   Lac, C., Pinty, J.-P., and Schwarzenböck, A.: Evaluation of the two-moment scheme
613   LIMA based on microphysical observations from the HyMeX campaign, Quarterly
614   Journal of the Royal Meteorological Society, 144(714), 1398-1414, 2018.

615 Sundqvist, H.: A parameterization scheme for non-convective condensation including
616   prediction of cloud water content. Q. J. R. Meteorol. Soc. 104, 677–690, 1978.

617 Tiedtke, M. : Representation of clouds in large-scale models. Mon. Weather Rev. 121,
618   3040–3061, 1993.

619 Wang, C. C., Chiou, B. K., Chen,G. T. J., Kuo, H. C., and Liu, C. H.: A numerical study of
620   back-building process in a quasistationary rainband with extreme rainfall over
621   northern Taiwan during 11–12 June 2012, Atmos. Chem. Phys., 16(18), 12359-

622   12382, 2016.

623 Yoshimura, K., Kanamitsu, M., Noone, D., and Oki, T.: Historical isotope simulation
624   using Reanalysis atmospheric data, J. Geophys. Res., 113(D19),
625   https://doi.org/10.1029/2008JD010074, 2008.

626 Yoshimura, K., Kanamitsu, M., and Dettinger, M.: Regional downscaling for stable water
627   isotopes: A case study of an atmospheric river event, J. Geophys. Res., 115,
628   D18114,https://doi.org/10.1029/2010JD014032, 2010.

629 Yoshimura, K.: Stable water isotopes in climatology, meteorology, and hydrology: A
630   review. J. Meteor. Soc. Japan, 93, https://doi.org/10.2151/jmsj.2015-036, 2015.

631 Yurtsever, Y., and Gat, J. R.: Atmospheric waters, of IAEA (ed), Stable Isotope Hydrology:
632   Deuterium and Oxygen-18 in the Water Cycle. Vienna: IAEA, 103-142, 1981.

633 Zwart, C, Munksgaard, N. C., Protat, A., Kurita, N., Lambrinidis, D., and Bird, M. I.: The
634   isotopic signature of monsoon conditions, cloud modes, and rainfall type.
635   Hydrological Processes, 32, 2296–2303, 2018.

636

637

638

639

640

641   Table 1. Description of the six numerical experiments conducted in this study.

642

Abbreviation	Description
CTRL	All processes are included.
EQ	The isotopic fractionation between different phases is in thermodynamic equilibrium.
NoIce	The isotopic fractionation between solid and other phases is the same as that of liquid and other phases (i.e., assuming the vapor pressure of solid HDO is the same as that of liquid HDO).
NoLnd	The initial δD over land is set to be the same as those over the ocean.
NoVh	The initial δD in the free troposphere was equal to that in the planetary boundary layer (i.e., no vertical gradient).
NoFrac	No isotopic fractionation considered in cloud microphysical processes (i.e., HDO is treated as a tracer).

643

644
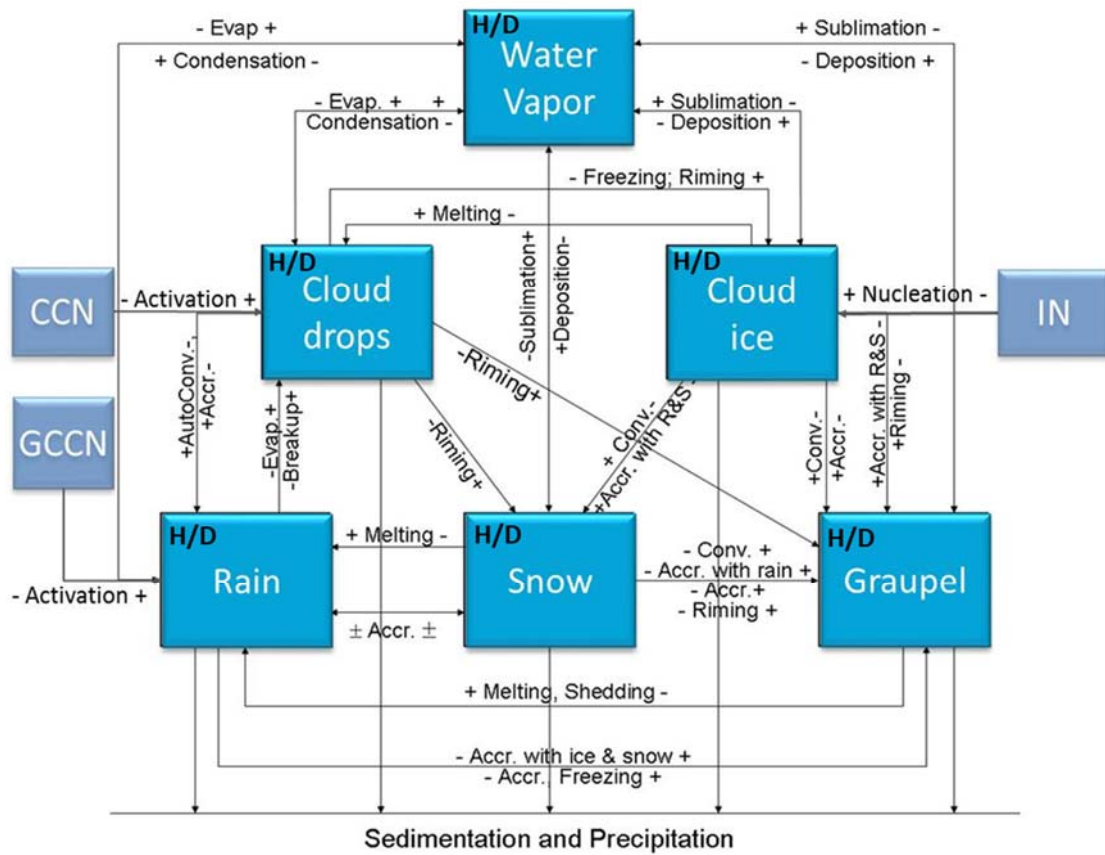
645

646   Figure 1. Schematics of the modified NTU scheme. The blue boxes are the hydrometeor

647   categories considered in the model, and the H/D indicated that both H_2O and HDO are

648   included. The arrows represent the microphysical conversion processes; and the light

649   blue boxes represent aerosol categories, including cloud condensation nuclei (CCN),

650   giant CCN (GCCN) and ice nuclei (IN). (Figure modified from *Cheng et al*. 2010)

651

652

653
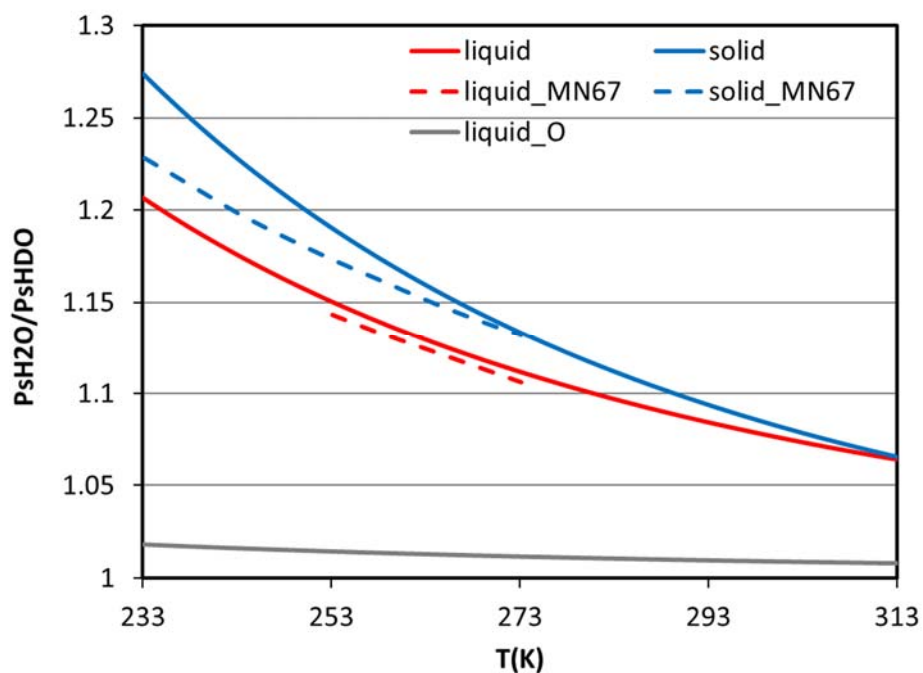
Figure 2. The ratio between saturation pressure of H_2O and HDO in different phases (liquid: red line, solid: blue line) at different temperatures. The grey line is the ratio of ^{18}O based on Horita and Wesolowski (1994). The dash lines are the formulas from Merlivat and Nief (1967).

659

660

661
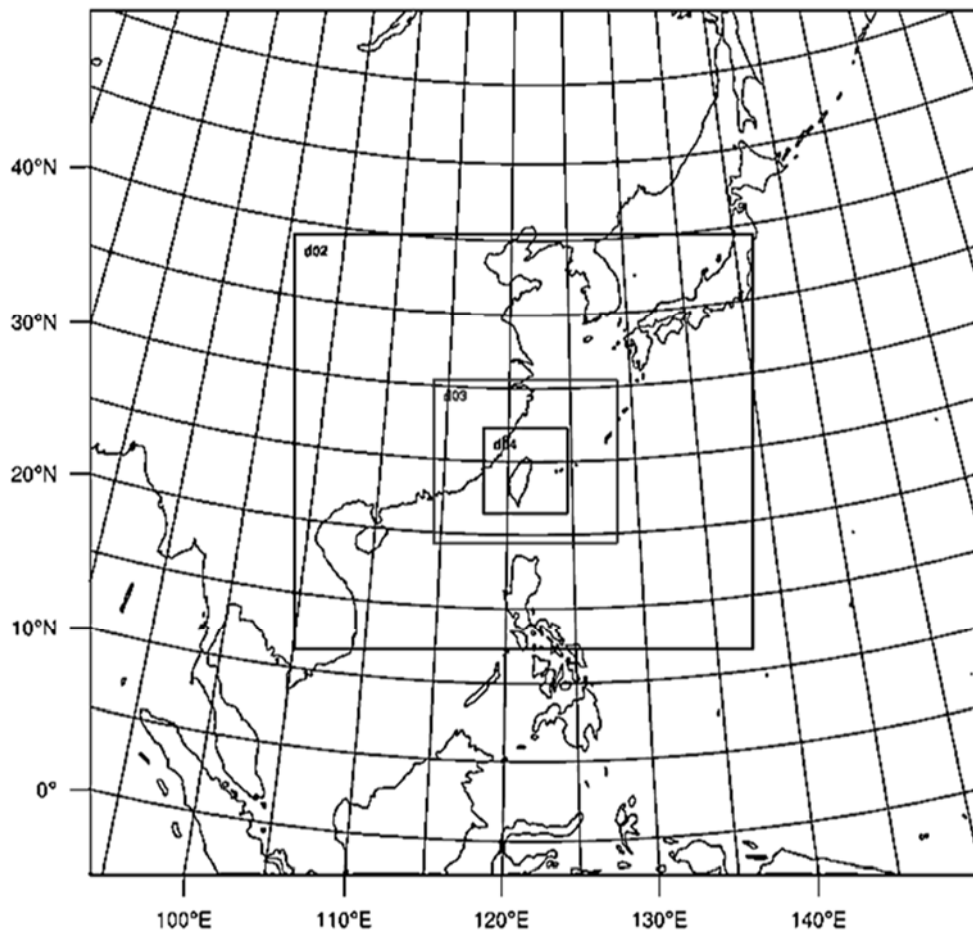
662

663 Figure 3. Map of the model domains for the simulations in this study. The resolutions

664 are 81, 27, 9 and 3 km in the outmost, 2nd, 3rd, and inmost domains, respectively.

665

666
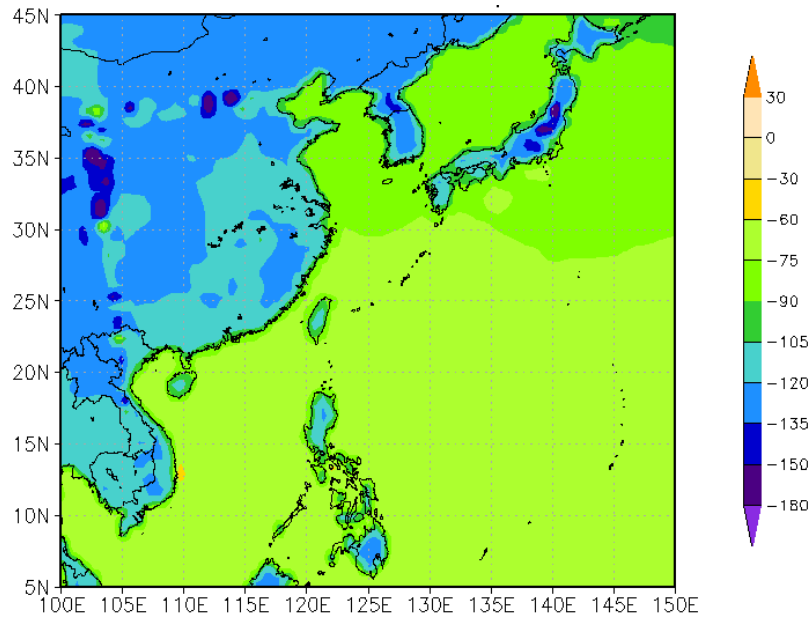
667   (a)
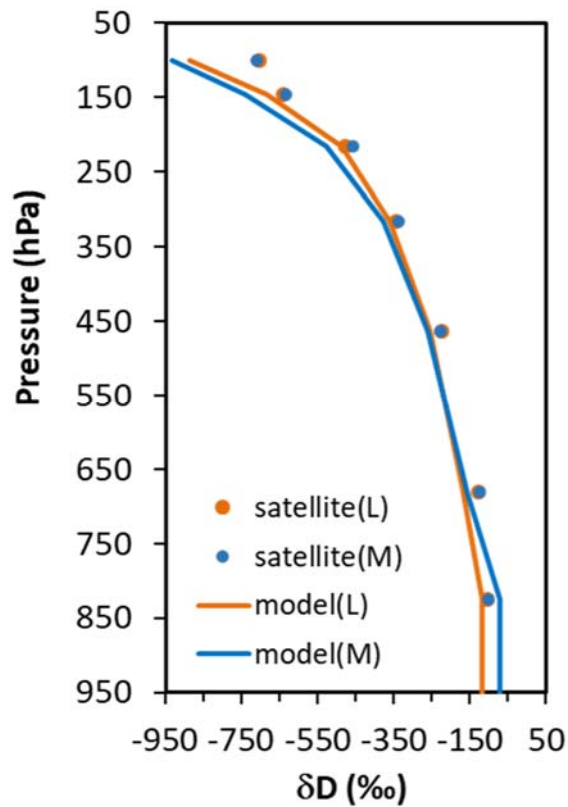
668   (b)

669   Figure 4. The initial distribution of water vapor δD (in ‰). (a) Surface distribution in

670   the coarse domain; (b) water vapor δD vertical profiles fitted from satellite data (dots).

671   Orange is for land (L), and blue is for marine (M)

672
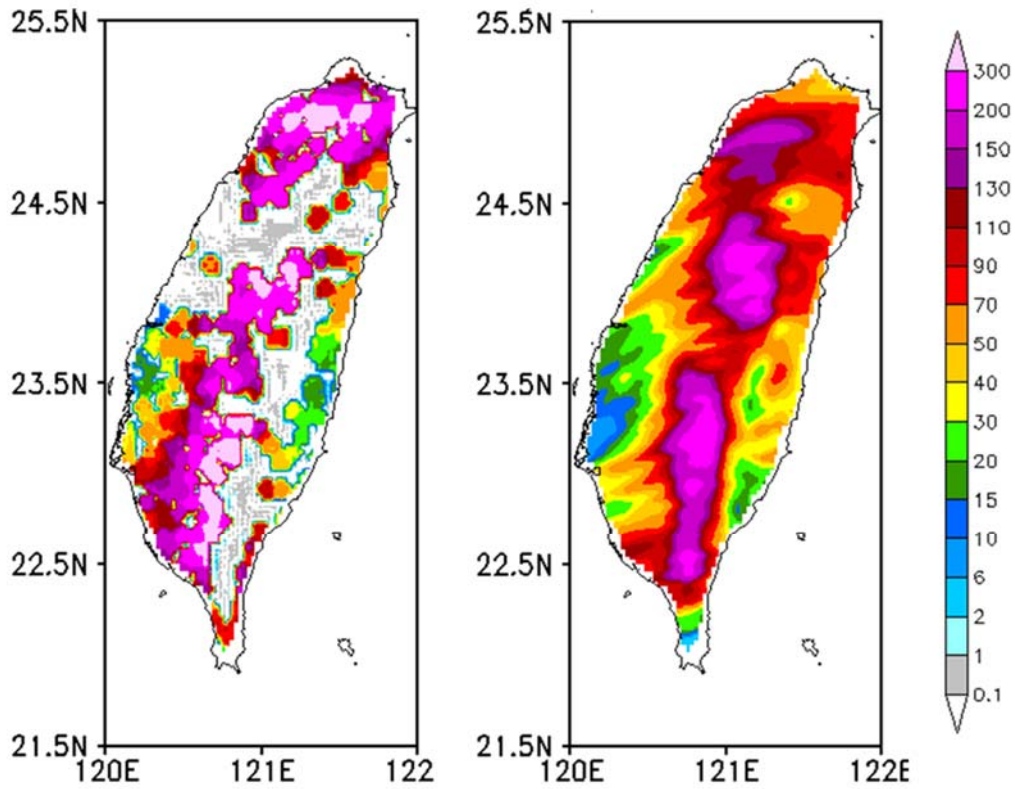
673   (a)

674
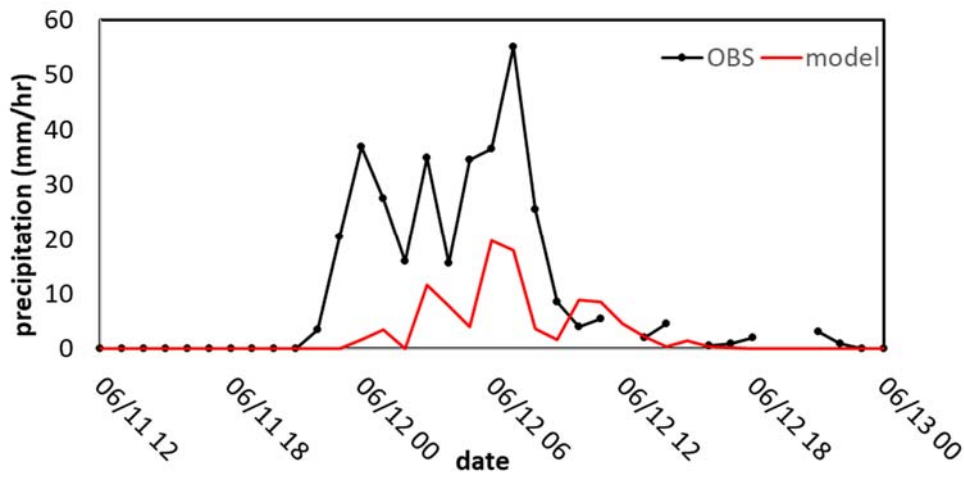
675   (b)

676

677   Figure 5. (a) Comparison between observed (left) and simulated (right) accumulated

678   precipitation (mm/hr) in Taiwan on 12 June 2012. Mark N and A denotes the location

679   of NTU and AS.   (b) Simulated (red line) and observed (black line) precipitation

680   (mm/hr) at Taipei station on 11-13 June 2012.

681

682

683
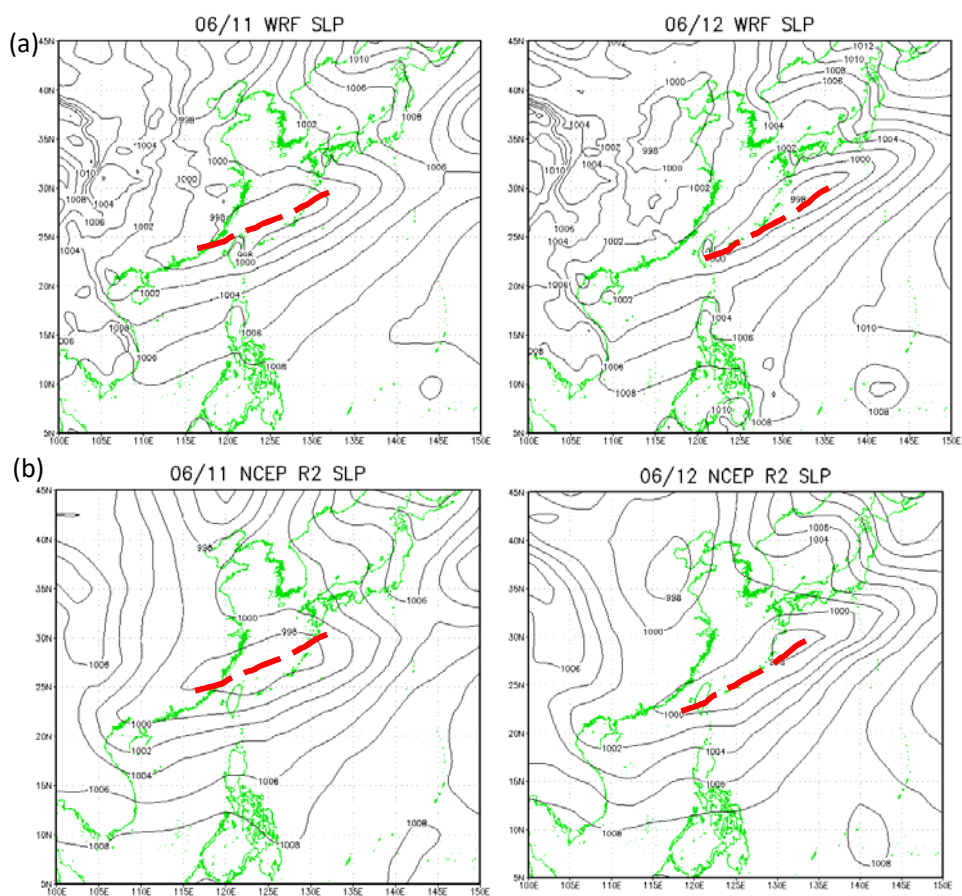
Figure 6. Comparison of (a) simulated sea level pressure (hPa) with (b) the NCEP
reanalysis data at 08:00 LST on 11 June (left) and 12 June (right), 2012. Frontal
position is indicated by the red dashed lines.

687

688

689
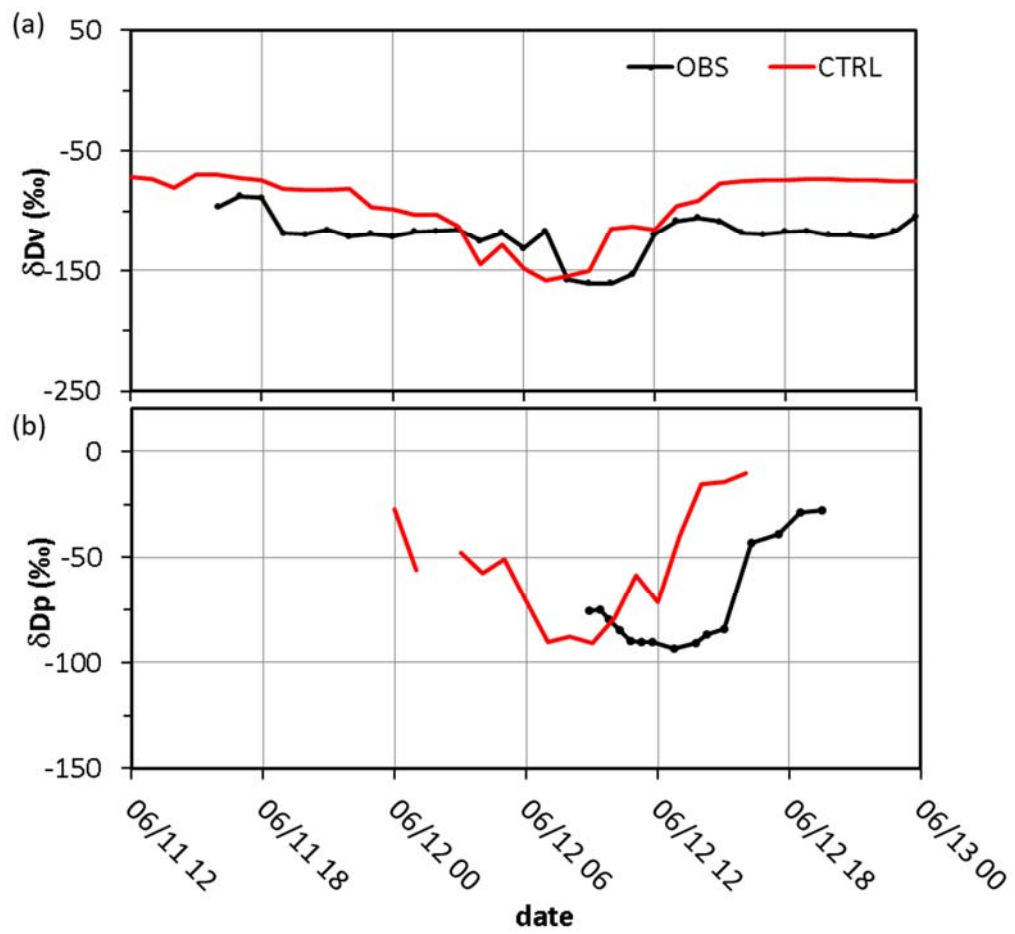
Figure 7. Simulated (CTRL: red line) and observed (OBS: black line) (a) water vapor

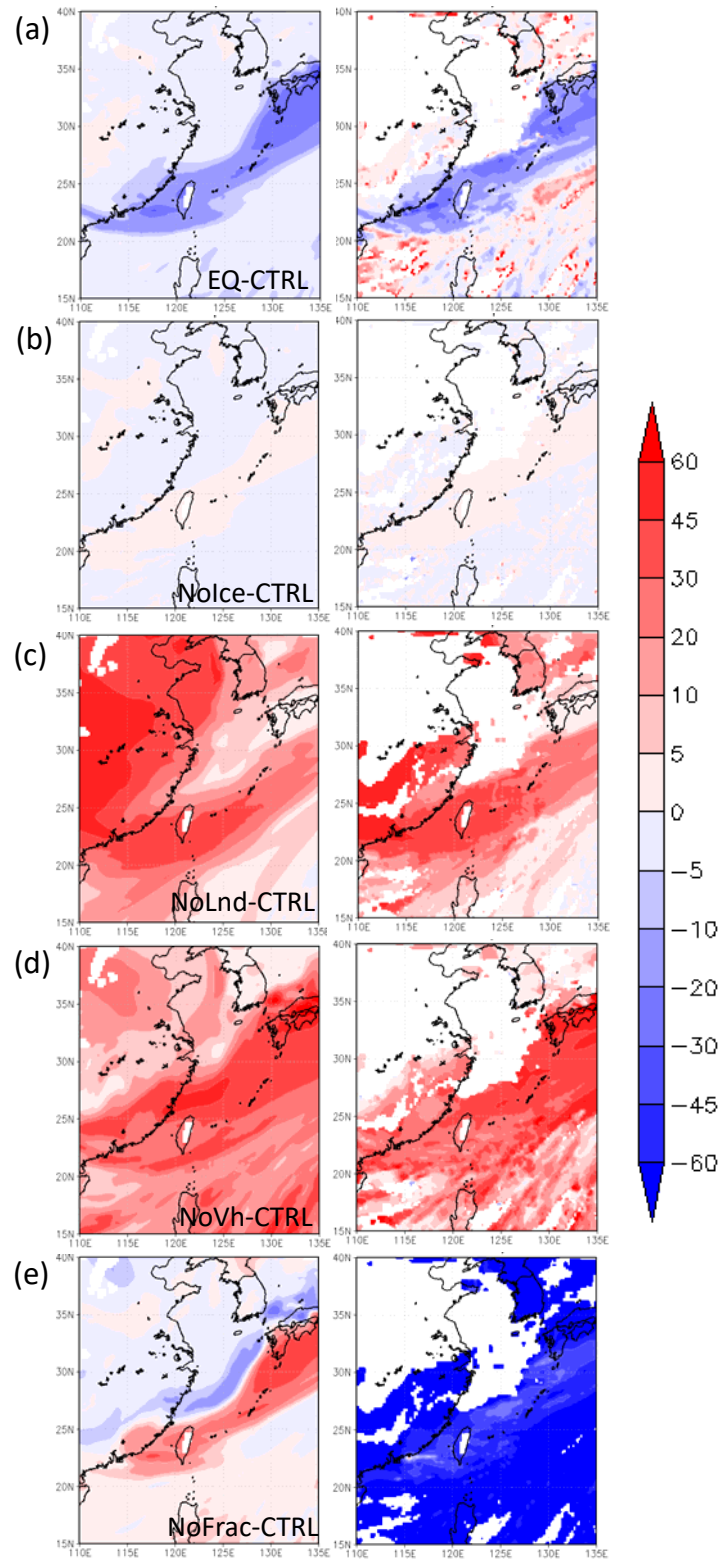δDv (in ‰) at AS and (b) precipitation δDp (in ‰) at NTU on 11-13 June 2012.

692

693
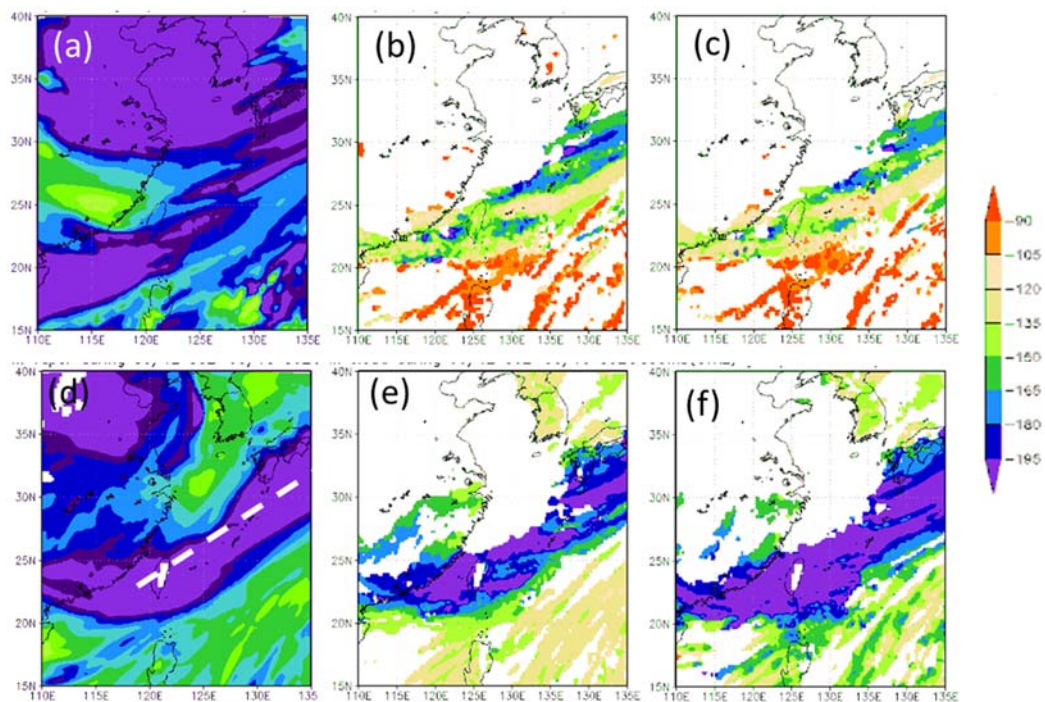
694

695 Figure 8. Simulated δD (in ‰) of water vapor (left), liquid-phase condensates
696 including cloud- and rainwater (middle), and ice-phase condensates, including cloud
697 ice, snow, and graupel (right) in the CTRL run at 500 hPa (a-c) and 850 hPa (d-f) on 12
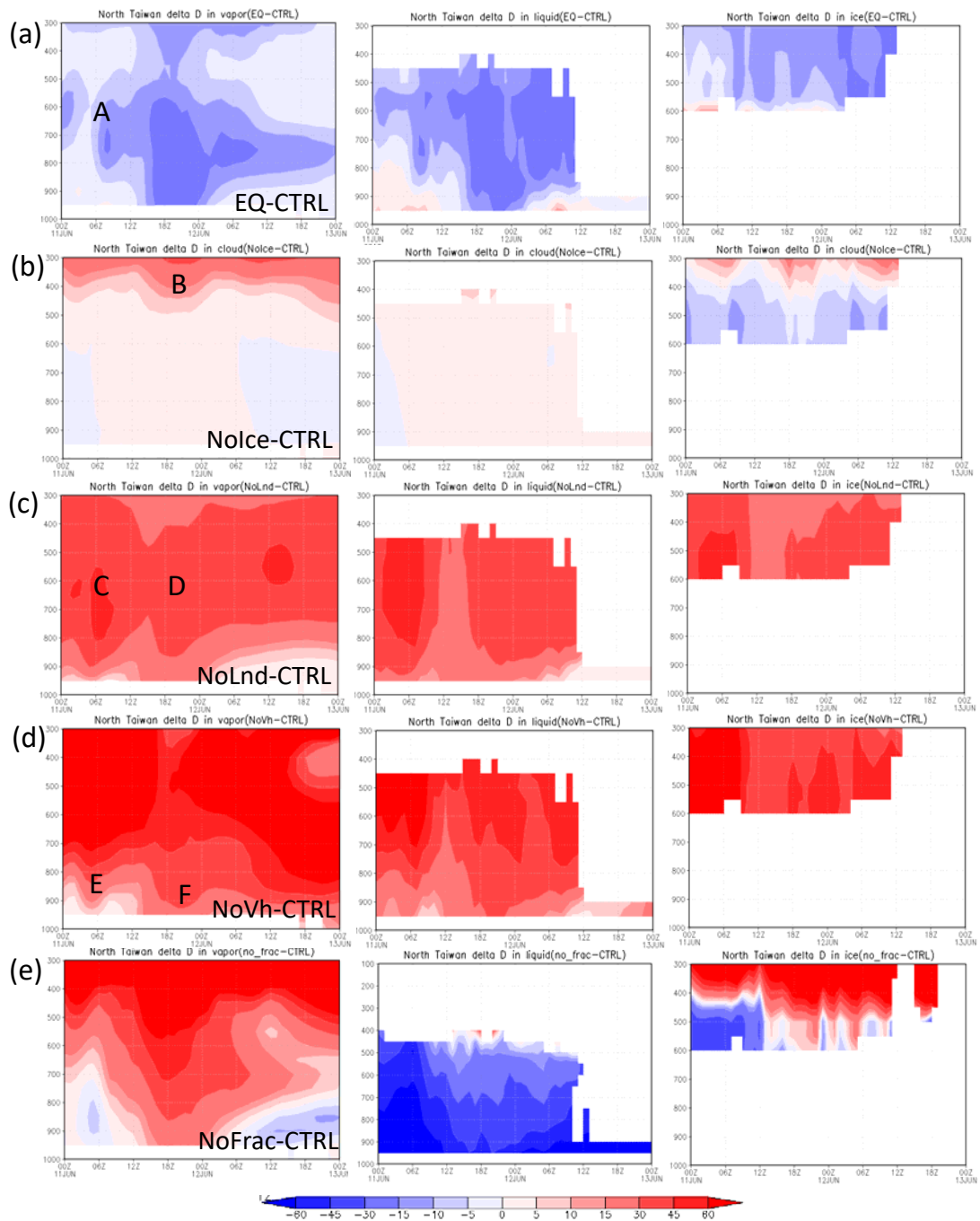698 June 2012.

699

700
701 Figure 9. Difference in simulated δD (in ‰) of water vapor (upper) and liquid-phase
702 condensates, including cloud- and rainwater (lower), between CTRL and other runs: (a)
703 EQ-CTRL, (b) NoIce-CTRL, (c) NoLnd-CTRL, and (d) NoVh-CTRL, and (e) NoFrac-CTRL, at
704 850 hPa on 12 June 2012.
705

Figure 10. Time evolution of the vertical distribution of simulated water vapor δD (left), liquid-phase water (cloud water and rainwater; middle), and ice-phase water (including cloud ice, snow and graupel; right) over Northern Taiwan (121-123°E, 25-27 °N) in different simulations: (a) EQ-CTRL, (b) NoIce-CTRL, (c) NoLnd-CTRL, (d) NoVh-CTRL,and (e) NoFrac-CTRL on 11-12 June 2012.   The ordinate is pressure (hPa), and abscissa is time.
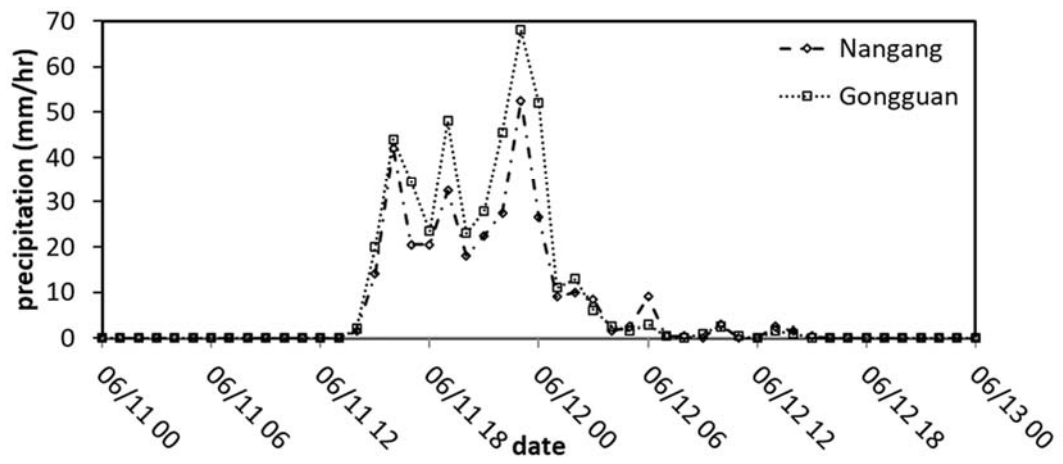
715
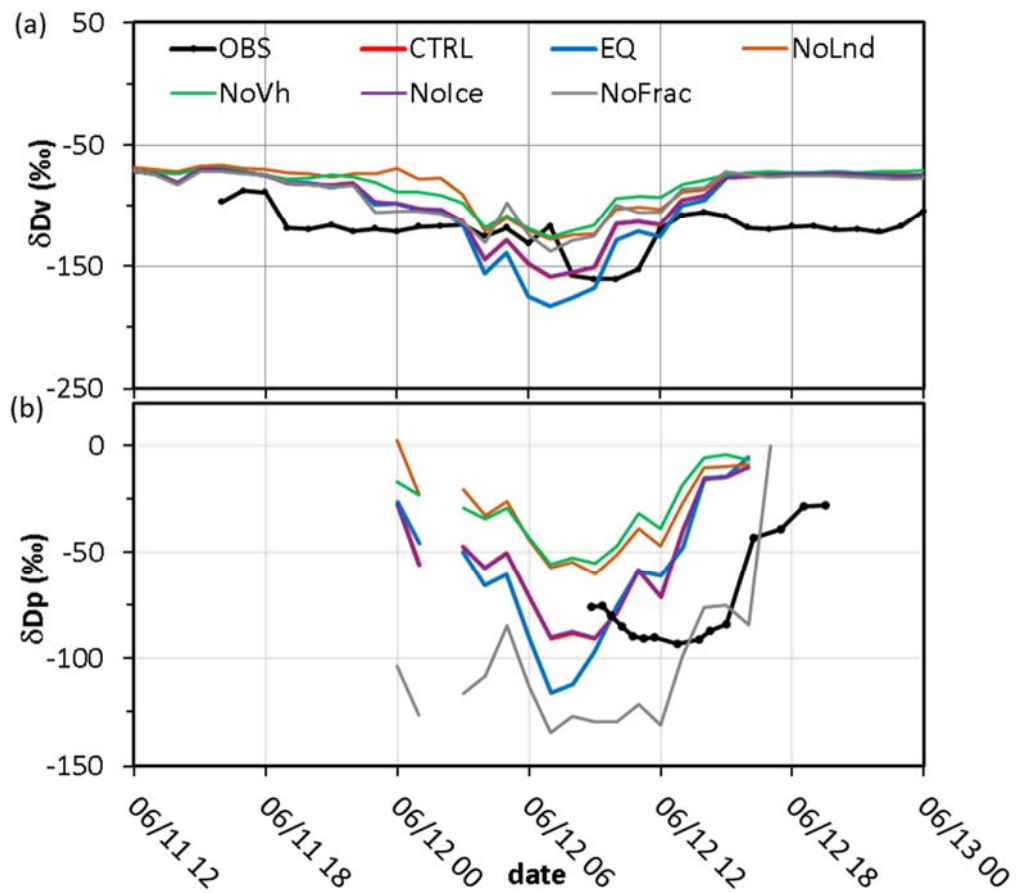
Figure 11. Same as Fig. 7 but for sensitivity simulations: the control run (CTRL, red line),
thermodynamic equilibrium run (EQ, blue line), no-ice run (NoIce, purple line), no-land
run (NoLnd, orange line), constant initial vertical profile run (NoVh, green line), and no
fractionation run (NoFrac, grey line).

720

721

722

723 Figure 12. Precipitation (mm/hr) at NanGang (dash line) and GongGuan (dot line)

724 Stations on 11-13 June 2012.

725

726

727